Regularized Iterative Reconstruction for Undersampled BLADE and Its Applications in Three-point Dixon Water–fat Separation

Qiang He,[1]* Dehe Weng,[2,3] Xiaodong Zhou,[1,3] and Cheng Ni[1]

In MRI, the suppression of fat signal is very important for many applications. Multipoint Dixon based water–fat separation methods are commonly used due to its robustness to B_0 homogeneity compared with other fat suppression methods, such as spectral fat saturation. The traditional Cartesian *k*-space trajectory based multipoint Dixon technique is sensitive to motion, such as pulsatile blood flow, resulting in artifacts that compromise image quality. This work presents a three-point Dixon water–fat separation method using undersampled BLADE (aka PROPELLER) for motion robustness and speed. A regularized iterative reconstruction method is then proposed for reducing the streaking artifacts coming from undersampling. In this study, the performance of the regularized iterative reconstruction method is first tested by simulations and on MR phantoms. The performance of the proposed technique is then evaluated in vivo by comparing it with conventional fat suppression methods on the human brain and knee. Experiments show that the presented method delivers reliable water–fat separation results. The reconstruction method suppresses streaking artifacts typical for undersampled BLADE acquisition schemes without missing fine structures in the image. Magn Reson Med 65:1314–1325, 2011. © 2011 Wiley-Liss, Inc.

Key words: sparse sampling; water–fat separation; BLADE; regularized iterative reconstruction

In MRI, fat suppression is very important for many clinical applications. When imaging anatomies with short T_1 species surrounded by fatty tissue, the fat may obscure a possibly underlying pathology unless it is suppressed in the MR images.

Several methods for fat suppression have been proposed over the past decades (1–6). Fat saturation (fatsat) and water excitation are commonly used. Both methods exploit the resonance frequency difference between fat and water and their performance is limited by field inhomogeneities. This is especially so at high fields. Another technique is short TI recovery (STIR), where an inversion pulse is applied and its inversion time is set to null fat (7–9). However, the STIR method alters the image contrast and is useful in specific applications only. Water and fat can also be separated using the multipoint Dixon technique. In this technique, multiple echoes are acquired at specific echo times (TEs). Because of the chemical shift of 3.5 ppm between protons bound in lipids and in water, the signals from these two distinct proton ensembles exhibit different phase offsets at the different TEs (10–17). The water and fat components in the image can then be separated by combining images from different TEs appropriately. The method is much less susceptible to B_0 or B_1 field inhomogeneities compared with other fat suppression methods.

The multipoint Dixon method can be incorporated into various MR imaging sequences. Cartesian *k*-space data sampling trajectories (10–21) are most often used, but such sampling schemes are known to be sensitive to motion, such as from pulsation, flow, and patient motion. The artifacts would degrade the image quality and may compromise the separation of water and fat signals in the imaging voxels. Recently, Huo et al. (22) proposed turboprop IDEAL. The method combines PROPELLER (the periodically rotated overlapping parallel lines with enhanced reconstruction, aka BLADE [not an acronym] in the MR systems from Siemens Healthcare Sector), which has good motion properties (23), with iterative decomposition of water and fat with echo asymmetry and least squares estimation (IDEAL) (21) for water–fat separation. Turboprop IDEAL Dixon technique reduces scan time by sampling multiple echoes within one TR interval.

In our work, we propose to use BLADE *k*-space sampling with a reduced number of blades together with a multipoint Dixon acquisition scheme using bipolar gradients readout to reduce the long scan time usually associated with the multipoint Dixon technique. As well known, images acquired with an undersampled BLADE trajectory using a conventional regridding reconstruction (23–26) would result in streaking artifacts. The streaking artifacts would have impact on the water–fat separation. To address this issue, we use an iterative reconstruction algorithm regularized by a total variation (TV) function and a wavelet base vectors to reconstruct the images at each TE before the water–fat separation. We refer this reconstruction method to the regularized iterative reconstruction.

First, in this article, we show the performance of the regularized iterative reconstruction for the BLADE schemes by simulations and phantom study. The three-point Dixon BLADE acquisition scheme was then implemented on a clinical scanner for phantom study and in vivo evaluation. Images from this new technique were

[1]Life Science and Technology School, Tongji University, Shanghai, China.
[2]Beijing MRI Center for Brain Research, Institute of Biophysics, Chinese Academy of Sciences, Beijing, China.
[3]Siemens Mindit Magnetic Resonance Ltd., Shenzhen, Guangdong, China.
*Correspondence to: Qiang He, Ph.D., Nanguolicheng Room 6N-1704, Xili, Nanshan District, 518055, Shenzhen, Guangdong, China.
E-mail: qiang.he@gmail.com
Received 21 April 2010; revised 21 September 2010; accepted 20 October 2010.
DOI 10.1002/mrm.22726
Published online 8 February 2011 in Wiley Online Library (wileyonlinelibrary.com).

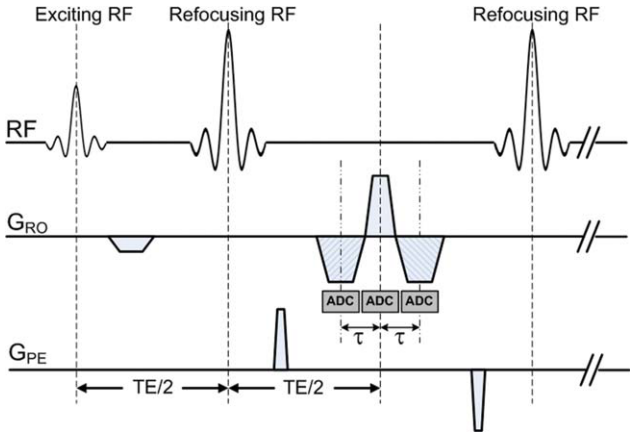

FIG. 1. Pulse sequence diagram for three-point Dixon. After each refocusing pulse, three echoes are sampled. The center echo is acquired at normal TE time. The time spacing between two consecutive echoes is τ. The raw data are filled along the blades in BLADE *k*-space trajectory. [Color figure can be viewed in the online issue, which is available at wileyonlinelibrary.com.]

compared with images, from a regular TSE sequence-based three-point Dixon method, from spectral fat-saturation, and from a regridding reconstruction based BLADE Dixon method, to show the effectiveness of the water–fat separation. Finally, we discuss the advantages and limitations of the proposed method.

MATERIALS AND METHODS

Data Acquisition

We modified a standard Turbo Spin-Echo (TSE) BLADE sequence by adding two more echo acquisitions before and after the normal echo with bipolar readout gradients after each refocusing radiofrequency pulse, so that in total three echoes are acquired for the water–fat separation, as shown in Fig. 1. This approach is similar to that of Glover and Schneider (11), except that echoes are now sampled along the blades rather than in a Cartesian *k*-space trajectory. In the implementation, all refocusing pulses have the same flip angle and can be user defined.

The three echoes collected with the bipolar readout gradients have TEs of TE/2 $-$ τ, TE/2, and TE/2 $+$ τ, where τ is the time spacing between two consecutive echoes. It can be adjusted to select specific phase offsets between the signals from water and fat, e.g., ($-\theta$, 0, θ). The three distinct signals acquired can be represented as (12):

$$\begin{aligned} S_{-1} &= \left(\mathrm{W} + \mathrm{F}e^{-i\theta}\right)e^{i(\phi_0-\phi)} \\ S_0 &= (\mathrm{W} + \mathrm{F})e^{i\phi_0} \\ S_{+1} &= \left(\mathrm{W} + \mathrm{F}e^{i\theta}\right)e^{i(\phi_0+\phi)}, \end{aligned} \quad [1]$$

where W and F denote the water and fat components in the tissue, respectively. ϕ_0 is a common phase offset resulting from radiofrequency penetration effects and other system related phase shifts inside the object and is independent of the chemical shift. θ is the phase difference between the central echo S_0 and the first and third echo (S_{-1} and S_{+1}) arising from the chemical shift between water and lipid bound protons. The phase ϕ arises from the inhomogeneity of the main magnetic field, ΔB_0, during the echo spacing time τ. That is, $\phi = 2\pi\cdot\gamma\cdot\Delta B_0\cdot\tau$.

During acquisition, the echoes are sampled along a BLADE trajectory and are sorted in three distinct *k*-spaces k_{-1}, k_0, and k_{+1}, corresponding to their TEs. The echo train length (ETL) of the sequence defines the number of phase-encoding lines within each blade. The blades are rotated around the *k*-space center with an angle increment $\alpha = \pi/N_\mathrm{B}$, where N_B is the total number of blades used. When the *k*-space is fully sampled by BLADE (23,26),

$$N_\mathrm{B} = \frac{\pi \cdot N}{2 \cdot \mathrm{ETL}} \quad [2]$$

Here, N is the number of data points in the readout direction. In this article, we let UR (undersampling rate) be the acceleration rate coming from the undersampling of the BLADE *k*-space by reducing the number of blades. Thus, UR $= N_\mathrm{Bf}/N_\mathrm{Bu}$. N_Bf stands for the number of blades when fully sampled and N_Bu for the one when undersampled.

For perfect reconstruction with a conventional regridding methods, the BLADE sampling patterns shall satisfy Eq. 2. Its scan time is about 50% longer than the conventional Cartesian sampling scheme because of oversampling around the *k*-space center.

Image Reconstruction Algorithm

Figure 2 shows the proposed image reconstruction algorithm applied to each of the three individual echoes, followed by the water–fat separation computation. When phased array coils are used, data from each individual coil element are combined using an adaptive coil combine algorithm (27) into images before the water–fat separation.

Regularized Iterative Image Reconstruction for Each Echo

It was recently found that with appropriate reconstruction algorithms, images can be reconstructed from sparsely sampled data (28,29). The sparse sampling method has then found relevance in MRI (30). Chang et al. and Block et al. (31,32) applied this idea in the reconstruction of undersampled radial *k*-space data, using a TV approach and a wavelet sparse representation transformation. They found the approach very useful in suppressing streaking artifacts typical in the reconstruction of undersampled radial *k*-space sampling. Liu et al. (33) applied a TV function regularized iterative reconstruction with an additional Bregman iteration for a sensitivity encoding parallel imaging algorithm and demonstrated good performance in removing aliasing artifacts and recovering fine object structures. Inspired by these works, we apply this technique to an undersampled BLADE *k*-space trajectory and combine it with the Dixon water–fat separation technique for scan time reduction. Because of the need for phase information in the water–fat separation algorithm, our algorithm works on complex images.

Following the formulation of Block et al. (31), the measured data from all blades for each echo can be

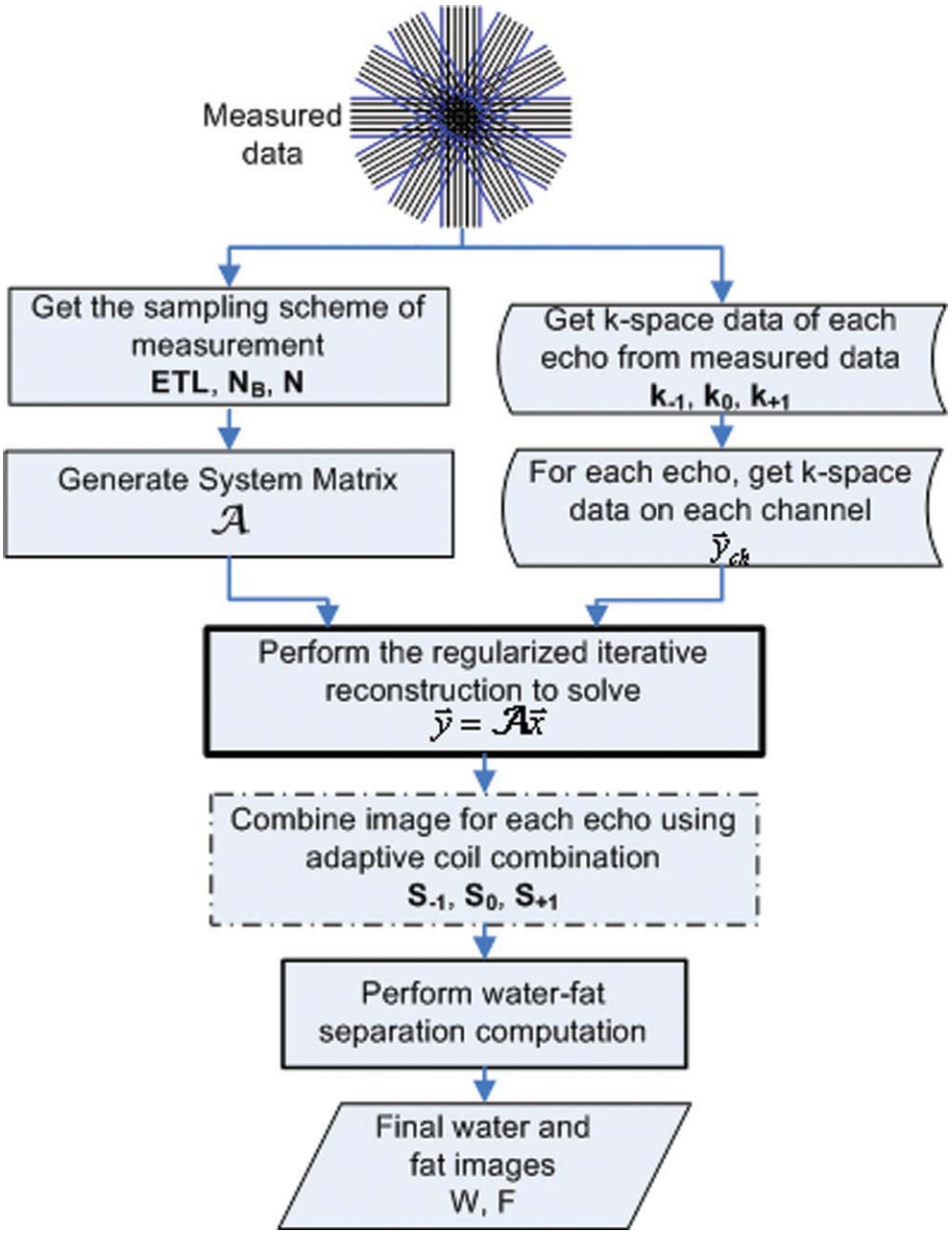

FIG. 2. Workflow of the proposed method for an undersampling TSE BLADE three-point Dixon. The workflow consists of two main steps, the regularized iterative reconstruction, and the water–fat separation computation. [Color figure can be viewed in the online issue, which is available at wileyonlinelibrary.com.]

stacked into a vector $\vec{y}$ with $N \times N_B \times$ ETL samples from each receiving channel. The spatial encoding process can be written as a linear operator, $\mathcal{A}$, which is called system matrix, as

$$\vec{y} = \mathcal{A}\vec{x}. \quad [3]$$

The image reconstruction process is the estimation of the image vector $\vec{x}$ with $N \times N$ pixel elements from the measured data $\vec{y}$ by solving the set of linear equations in Eq. 3. This set of equations is both very large and ill-posed because of the image matrix size and undersampling. Hence, iterative solution is more appropriate than closed form solutions (31).

In the iterative algorithm, the l_2-norm of the residuum of the estimated image with the system matrix $\mathcal{A}$ from the measured data $\vec{y}$ can be used as a measure to show how close the reconstructed image is to the original image. That is, the algorithm seeks for minimizing the l_2-norm of the residuum (31):

$$\vec{x} = \underset{\vec{x}}{\operatorname{argmin}} \frac{1}{2} \|\mathcal{A}\vec{x} - \vec{y}\|_2^2. \quad [4]$$

The solution of the ill-posed Eq. 2 can be improved by introducing weighted penalty functions:

$$\vec{x} = \underset{\vec{x}}{\operatorname{argmin}} \left\{ \frac{1}{2} \|\mathcal{A}\vec{x} - \vec{y}\|_2^2 + \sum_i \lambda_i R_i(\vec{x}) \right\}, \quad [5]$$

where the $R_i(\cdot)$ is the penalty function, and the λ_i is the corresponding weighting factor, which are adjustable coefficients according to the properties of the measured data, e.g., the signal-to-noise ratio (SNR) of image and the desired spatial resolution. The penalty functions are

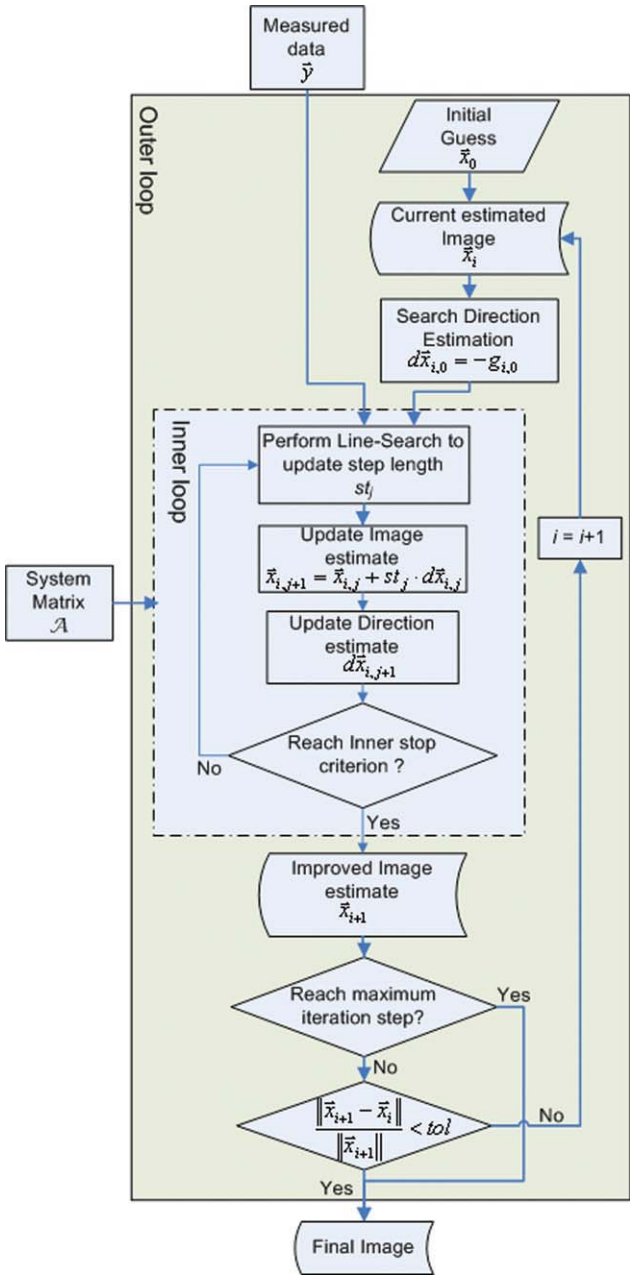

FIG. 3. Workflow of the regularized iterative reconstruction. System matrix A and measured data are inputs. Two main loops, the inner loop (with index *j*) and the outer loop (with index *i*), are included in the workflow. The output of reconstruction is complex image, which is used for water–fat separation, as in Fig. 2. In the inner loop, the matrix-vector multiplications with A and its adjoint matrix $\mathcal{A}^{\#}$ are performed. [Color figure can be viewed in the online issue, which is available at wileyonlinelibrary.com.]

selected according to the a priori information about the imaged objects, which is often distributed sparsely in the tissues (31,32). In this algorithm, we use two penalty functions, namely the TV function and the wavelet function. The TV function has been successfully used for image restoration from noisy data (34) and is suitable to describe the a priori knowledge for MR images (31). The TV function for two-dimensional images is

$$\mathrm{TV}(\vec{x}) = \sum \sqrt{|\nabla_x \vec{x}|^2 + |\nabla_y \vec{x}|^2}, \qquad [6]$$

where ∇_x and ∇_y denote the gradient along *x* and *y* direction in two-dimensional images, respectively, and $|\cdot|$ is the complex modulus. The wavelet is commonly used for the image compression for storage and recovering the digital images (35). Thus, Eq. 5 can be rewritten as:

$$\vec{x} = \underset{\vec{x}}{\mathrm{argmin}} \left\{ \frac{1}{2} \|\mathcal{A}\vec{x} - \vec{y}\|_2^2 + \lambda_1 \mathrm{TV}(\vec{x}) + \lambda_2 W(\vec{x}) \right\} \qquad [7]$$

where $W(\cdot)$ is the wavelet function. In this work, the Daubechies-6 wavelet (36) is used.

To find the optimal solution for Eq. 7, two iteration loops (the inner and outer loops) are employed in the iterative reconstruction procedure, as shown in Fig. 3. In the inner loop, the nonlinear conjugate gradient method is used in the estimation of the image. This is one iterative method and frequently used for the solution of linear systems (37). The conjugate gradient method consists of two steps. First, the search direction in the parameter space is estimated. It is then followed by the identification of a minimum of the function along this direction by means of a linear search. As shown in Fig. 3, the inner loop outputs the updated image estimate, which is delivered to the outer loop until the specified maximum number of iterations is reached or the stopping criterion is fulfilled. In this article, the stopping criterion was defined as $\|x_{i+1} - x_i\| / \|x_{i+1}\| <$ tolerance.

In the diagram of Fig. 3, the matrix-vector multiplication $\mathcal{A}\vec{x}$ is performed. The difference of $\mathcal{A}\,\vec{x}$ from the measured data $\vec{y}$ (i.e., residuum, $\mathcal{A}\vec{x} - \vec{y}$) is calculated to measure whether the image estimate $\vec{x}$ is good enough. If it is not good enough, the algorithm needs to know how to modify the image estimate so as to improve the match of the samples in the measured data. This information is obtained by calculating the residuum back to the image domain using the matrix-vector multiplication with $\mathcal{A}^{\#}$ (the adjoint matrix to $\mathcal{A}$) (31). These calculations are performed when looping through the conjugate gradient method. To improve the speed and the numerical accuracy, the nonuniform fast Fourier transform approximations with min–max interpolations are used as the operator for the matrix-vector multiplications (38).

For each individual receiving coil channel, this regularized iterative reconstruction algorithm is applied to each of the three raw data sets from the three acquired echoes. Before the water–fat separation, the images from each of the three echoes are combined from all receiving channels using an adaptive coil combination algorithm (27). The water–fat separation calculation is performed using similar algorithm proposed by Glover and Schneider (11), except that the region growth algorithm optimized by Zhou et al. (39) was used for phase unwrapping in local field inhomogeneity calculation.

EXPERIMENTS

Simulations

MATLAB (R2009b, The Mathworks, MA) running on PC (4GB RAM, AMD Athlon II X4 635 CPU) was used in both the numerical phantom synthesis and algorithm

Table 1
Downsampling Blade Patterns for Phantom Studies

Sampling pattern	Blade used for reconstruction	UR	Scan time (sec)
For the resolution phantom[a]			
Case 1 (full sampling)	Blade #1 to #27	1	81
Case 2 (1/3 sampling)	Blade #(3K + 1), K = 0, . . ., 8	3	27
Case 3 (Nonuniform sampling)	Blade #4 to #11, blade #15 to #24	1.5	54
For the oil–water phantom[b]			
Case 1 (full sampling)	Blade #1 to #22	1	110
Case 2 (1/2 sampling)	Odd blades	2	55
Case 3 (1/4 sampling)	Blade #(4K + 1), K = 0. . .5	3.67	30

[a]TR = 3000 msec, TE = 100 msec, resolution = 256 × 256, field of view = 300 × 300 mm^2, ETL = 15, slice thickness = 5 mm, and 1 average.
[b]TR = 5000 msec, TE = 145 msec, resolution = 256 × 256, field of view = 170 × 170 mm^2, ETL = 19, slice thickness = 5 mm, and 1 average.

implementation. The latter used the free MATLAB package nonuniform fast Fourier transform (38).

A Shepp-Logan phantom with normalized intensity (minimum pixel value = 0 and maximum = 1.0) was used in the simulation. Zero mean white gaussian noise with two cases, variance of 0.001 (SNR = 9.4) and variance of 0.0, were added to the numerical phantom. It was sampled using the BLADE trajectory with 17 phase-encoding lines in each blade (i.e., ETL = 17). The reconstruction algorithm was tested using a fraction of the *k*-space data, by changing the number of blades from 24 (fully sampled) to 19, 12, 9, and then 6 (i.e., UR = 1, 1.4, 2, 2.7, and 4, respectively). The simulated data were reconstructed using the regridding method and the regularized iterative reconstruction.

Sequence Implementation

The sequence was implemented on a 1.5-T MRI scanner (MAGNETOM ESSENZA, Siemens, Shenzhen, China) with a maximum gradient of 30 mT/m and a maximum slew rate of 100 T/m/sec. The acquired data was reconstructed offline with MATLAB. Three-dimensional B_0 shimming was run before the raw data acquisition from phantoms and volunteers.

Phantom Experiments

A resolution phantom from the manufacturer was used. The phantom is filled with $NiSO_4{\cdot}5H_2O$ solution. The images were acquired with the implemented TSE BLADE sequence using an eight-channel receive-only head coil. Only one slice was acquired with 27 blades (ETL = 15, fully sampled), with scan time of 81 sec. Additional experiments were done by extracting data from the fully sampled data with different downsampling patterns to demonstrate the performance of the regularized iterative reconstruction method and the impact of the sampling pattern on the reconstruction quality. For better description of the sampling scheme, the blades were numbered in order of the actual scanning process, from #1 to #27. The scanning parameters and the downsampling patterns are shown in Table 1. The data were reconstructed with the conventional regridding method and the regularized iterative reconstruction method.

Another phantom fulfilled with oil and water was used to evaluate the performance of the proposed method for water–fat separation. The data was fully sampled with 22 blades (ETL = 19), using an eight-channel receive-only head coil. The scan time was 110 sec. The data were then downsampled from the full data set according to Table 1 case 2 and case 3. The same reconstruction method(s) in the resolution phantom study was used to generate three complex images, which were then used for the water–fat separation.

Volunteer Experiments

To evaluate the performance of the proposed algorithm in vivo, volunteer experiments were performed. Two anatomical positions were chosen:

1. The orbits of the eyes in the transverse slice orientation. This anatomy has two challenges: (a) strong susceptibility gradients around the structure resulting in large local B_0 inhomogeneities and (b) eye ball movement and fluid flow around the orbit during imaging introduce motion artifact. Good fat suppression in this region is usually difficult. An eight-channel receive-only head coil was used in signal reception.
2. The knee in an axial orientation. Images at this orientation were usually artifact prone because of pulsation of the blood vessels. An eight-channel receive-only extremity coil was used in signal collection.

Three sets of images were acquired for each location for image quality comparison: standard TSE with fat suppression, standard TSE with three-point Dixon, and TSE BLADE three-point Dixon sequence. Table 2 shows the imaging parameters used in the experiments.

Image reconstruction was done online for TSE with fatsat and TSE with three-point Dixon acquisitions. The

Table 2
Imaging Parameters Used for the In Vivo Experiments

	TSE with fatsat	TSE with 3pt Dixon	BLADE TSE with 3pt Dixon
For the orbit[a]			
TR/TE (msec)	5000/118	5000/100	5000/119
ETL	15	19	19
Echo spacing (msec)	n/a	2.37	2.37
Scan time (sec)	90	70	110 (22 blades)
Phase encoding	A≫P	A≫P	A≫P[b]
For the knee[c]			
TR/TE (msec)	5000/117	5000/117	5000/117
ETL	15	19	17
Echo spacing (msec)	n/a	2.37	2.37
Scan time (sec)	90	70	120 (24 blades)
Phase encoding	R≫L	R≫L	R≫L[b]

[a]Field of view = 300 × 300 mm^2, slice thickness = 8 mm, matrix = 256 × 256, refocusing flip angle = 180°, and 1 average.
[b]Due to the rotation of blades, the phase-encoding direction for the TSE BLADE 3-point Dixon are not the same as for the Cartesian trajectories.
[c]Field of view = 180 × 180 mm^2, slice thickness = 8 mm, matrix = 256 × 256, refocusing flip angle = 180°, and 1 average.

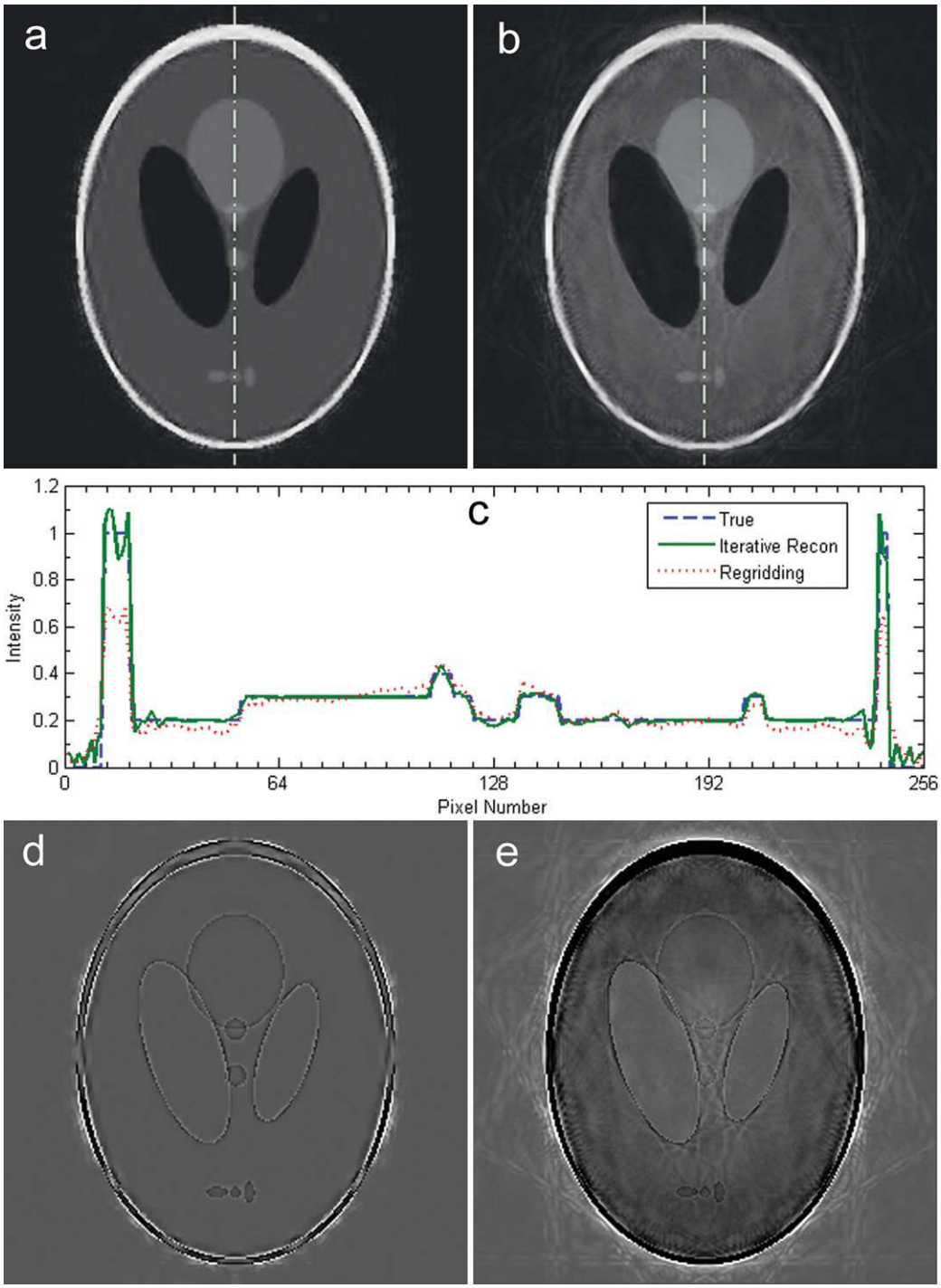

FIG. 4. The simulation results of the noisy-free Shepp-Logan phantom, using six blades. **a:** Image using regularized iterative reconstruction (with $\lambda_1 = 0.01$ and $\lambda_2 = 0.01$, 10 inner iterations and 8 outer iterations); **b:** image using the regridding method; **c:** profiles of true object (dash line), image a (solid line) and image b (dot line), along the dash–dot line shown in a and b; **d:** difference image of image a from the true object; **e:** difference image of image b from the true object. [Color figure can be viewed in the online issue, which is available at wileyonlinelibrary.com.]

measured data from the TSE BLADE sequence with three-point Dixon were reconstructed offline using MATLAB in two different ways: the regridding reconstruction and then the regularized iterative reconstruction. The raw data from different sampling schemes were obtained by subsampling the full data set.

RESULTS

Figure 4 shows the simulation results with the Shepp-Logan numerical phantom without white gaussian noise using six blades. For all three undersampling schemes used in the simulation, the images reconstructed using

Table 3
MSE of the Images of Noise-Free Simulation Using the Regularized Iterative Reconstruction and the Regridding Reconstruction

Number of blades	MSE with iterative method	MSE with regridding method
6 (UR = 4)	0.0026	0.0086
9 (UR = 2.7)	0.0019	0.0075
12 (UR = 2)	0.0015	0.0071
19 (UR = 1.3)	0.0005	0.0050
24 (full sampling)	0.0001	0.0033

Table 4
SNR of the Images With the Regularized Iterative Reconstruction and the Regridding Reconstruction

Number of blades	SNR with iterative method ($\lambda_1 = 0.001$)	SNR with iterative method ($\lambda_1 = 0.01$)	SNR with regridding
6	33.4	76.4	16.7
9	18.9	49.6	13.9
12	16.1	33.3	12.6
19	12.4[a]	19.2[a]	11.6
24	12.2	17.6	11.9

[a]SNR of the image changes with the weighting factor of TV and slightly with the number of iterations. For 19 blades, SNR = 13.6 (inner iteration = 10, outer iteration = 40, $\lambda_1 = 0.001$).

the regridding method have more streaking artifacts than the images obtained from the regularized iterative reconstruction algorithm, as shown in different images, i.e., Fig. 4d and e. The signal profile from Fig. 4c shows that at the sharp edges, i.e., the region where signal changes fast, signal from the regularized iterative method is much closer to the true values than that from the regridding method. Table 3 shows the mean square error (MSE) of the reconstructed images from the true object. The MSE of both reconstruction methods decrease with increasing number of blades. Both results suggest that the regularized iterative method recovers information better than the regridding algorithm even from the noisy data sets. At the sharp edges, the signal from the regularized iterative method also exhibits some kind of ringing artifact, though not severe. This may come from the edge preservation performance of the TV function.

Table 4 shows the local SNR of the true object (with white gaussian noise, zero mean and variance of 0.001) and the reconstructed images (with different number of blades) using the regularized iterative reconstruction (10 inner iterations and eight outer iterations), and the regridding method. The SNR of the results with $\lambda_1 = 0.01$ are higher than with 0.001. The SNR of the results with $\lambda_1 = 0.001$ are then higher than with the regridding method. These comparisons suggest that appropriate weighting factor shall benefit denoising for images. Another observation is that the SNR decreases when the number of blades increases. The SNR slightly increases with increasing number of iterations, as described by note a under Table 4.

Figure 5 shows the convergence curve of the normalized MSE (NMSE) using six blades, when $\lambda_1 = 0.01$ and $\lambda_2 = 0.01$, with 10 inner iterations. The true object is noise-free. The NMSE was calculated by normalizing MSE by the sum of the pixel values in the true object. It can be seen that NMSE decreases very fast initially and then slows down after about five iterations. It suggests that the algorithm converges more effectively in the first iterations, and the image quality shall not be improved significantly when further increasing the number of iterations. Therefore, in the reconstruction for the phantom studies and the volunteer experiments in this article, the number of outer iterations and inner iterations was set eight and 10 respectively.

In Fig. 6, the images of the resolution phantom are shown. The images were reconstructed using the undersampling schemes listed in Table 1. The spatial resolution of the images is 1.17 mm. The images from the regridding reconstructions (Fig. 6e–g) show streaking artifacts, which increases with UR. The sharp transitions between the signal and "holes" (signal void in the image) are better visualized in Fig.6b–d because of the improved streaking suppression from the regularized iterative reconstruction. To better understand the signal behavior around the small holes, the pixel intensities along the line marked in Fig. 6a are inverted and plotted for Fig. 6c and f (see Fig. 6h). Along the profile, peaks 1, 4, and 5 (counting from the left) of the dash–dot curve is higher than the ones of solid curve. The results show that the "holes" in the images reconstructed using the new method are better depicted.

The results from the water and oil phantom experiment are shown in Fig. 7. The profiles along the dotted line show that fat was well suppressed, as in Fig. 7g and h. Table 5 lists the ratio of water and remaining fat signals, together with the standard deviations (SDs) of remaining fat signals with various downsampling schemes (i.e., Table 1). Note that the water–fat signal ratios are almost the same, when images are reconstructed with the proposed method; whereas, this ratio using the regridding method decreases with increasing UR. The new method is more robust in fat suppression to downsampling schemes compared with the conventional regridding method. The increase of streaking artifact with UR from the regridding method may be an important reason for this result.

In Fig. 8, the volunteer orbit images acquired with various fat suppression methods are shown. The artifact due

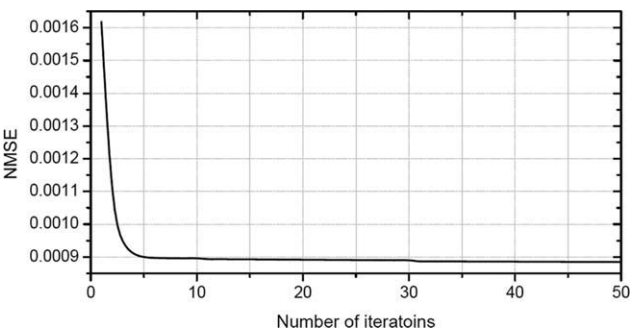

FIG. 5. The NMSE convergence curve of the regularized iterative reconstruction for the noise-free simulation. The NMSE decrease very fast at the first iterations and keep reducing slowly as the number of iterations increases.

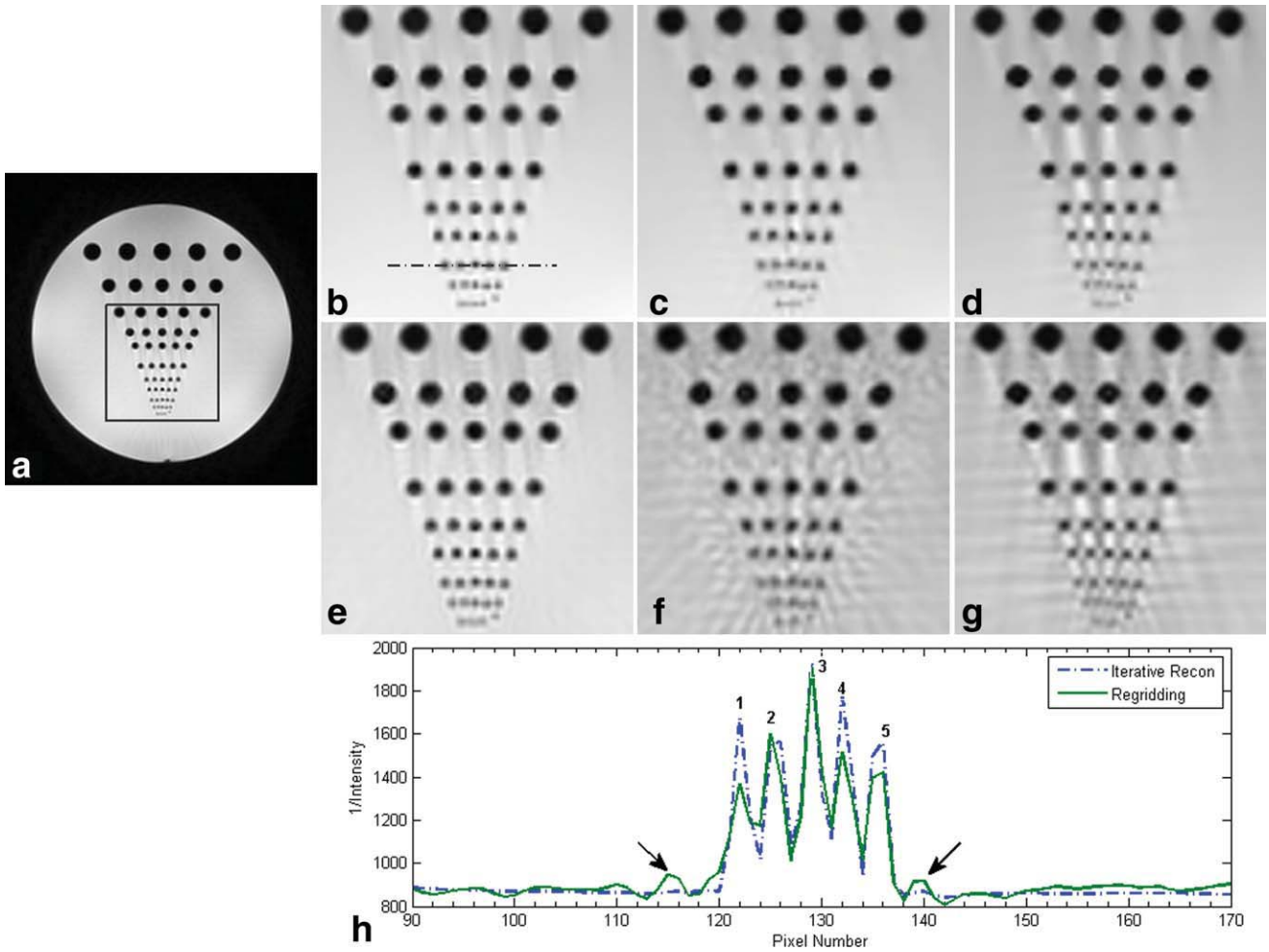

FIG. 6. The reconstruction results of the resolution phantom. **a:** Image using the regularized iterative reconstruction, with full sampling (ETL = 15 and 27 blades). The block in the solid box is zoomed and shown in figures **b–g**; **b–d:** Zoomed images using the regularized iterative method (with $\lambda_1 = 0.01$ and $\lambda_2 = 0.01$, 10 inner iterations and eight outer iterations), with full sampling, with 1/3 sampling and with nonuniform sampling, respectively; **e–g:** Zoomed image using the regridding reconstruction with the same sampling schemes in b–d; **h:** Profile of c and f along the dash–dot line shown in b. The spatial resolution of this row is 1 mm. The peak 1, 4, and 5 (counting from left) can be distinguished better in the profile using the regularized iteration method. Artifacts are shown as side peaks in the profile of f, as pointed by arrows. [Color figure can be viewed in the online issue, which is available at wileyonlinelibrary.com.]

to the motion of eye ball can be observed in phase-encoding direction in the Cartesian sampling scheme (Fig. 8a and e). With the regridding reconstruction, because of the streaking artifacts, the anatomies are not smooth and appear noisy (Fig. 8b–d). Some of artifacts can be easily recognized as small anatomies (e.g., cerebrospinal fluid) because of their relatively high intensity, as pointed by the arrows in Fig. 8c and d. The proposed method generated smooth structures in images (Fig. 8f–h).

Figure 9 presents the volunteer knee images. In Fig. 9a, because of the local B_0 inhomogeneities, fat was not suppressed perfectly in the regions pointed by the arrow. The pulsation artifacts are observed in the phase-encoding direction, as pointed by the v-type arrow. As shown in Fig. 9b–d and f–h, the similar results in the orbit images were observed, when using the proposed method and using the regridding method, i.e., the proposed method can suppress the streaking artifact better than the regridding method. However, when using the proposed method, slight blurring can be observed around the hyperintense water regions, as pointed by the arrows in Fig. 9f,g. This may come from the averaging effect of the interpolation in the nonuniform fast Fourier transform.

DISCUSSION

In this article, we proposed a robust method of water–fat separation combining a regularized iterative reconstruction for an undersampling TSE BLADE three-point Dixon acquisition. The regularized iterative reconstruction method performs better in the suppression of streaking artifacts when compared with a regridding method, resulting in improved resolution of small structures based on the same *k*-space data in the frequency domain. The reduced streaking artifact may also contribute to the small improvement in fat suppression with the regularized iterative reconstruction algorithm.

The resolution of both the proposed method and the regridding based method are limited by the high frequency information in the *k*-space data. Therefore, the

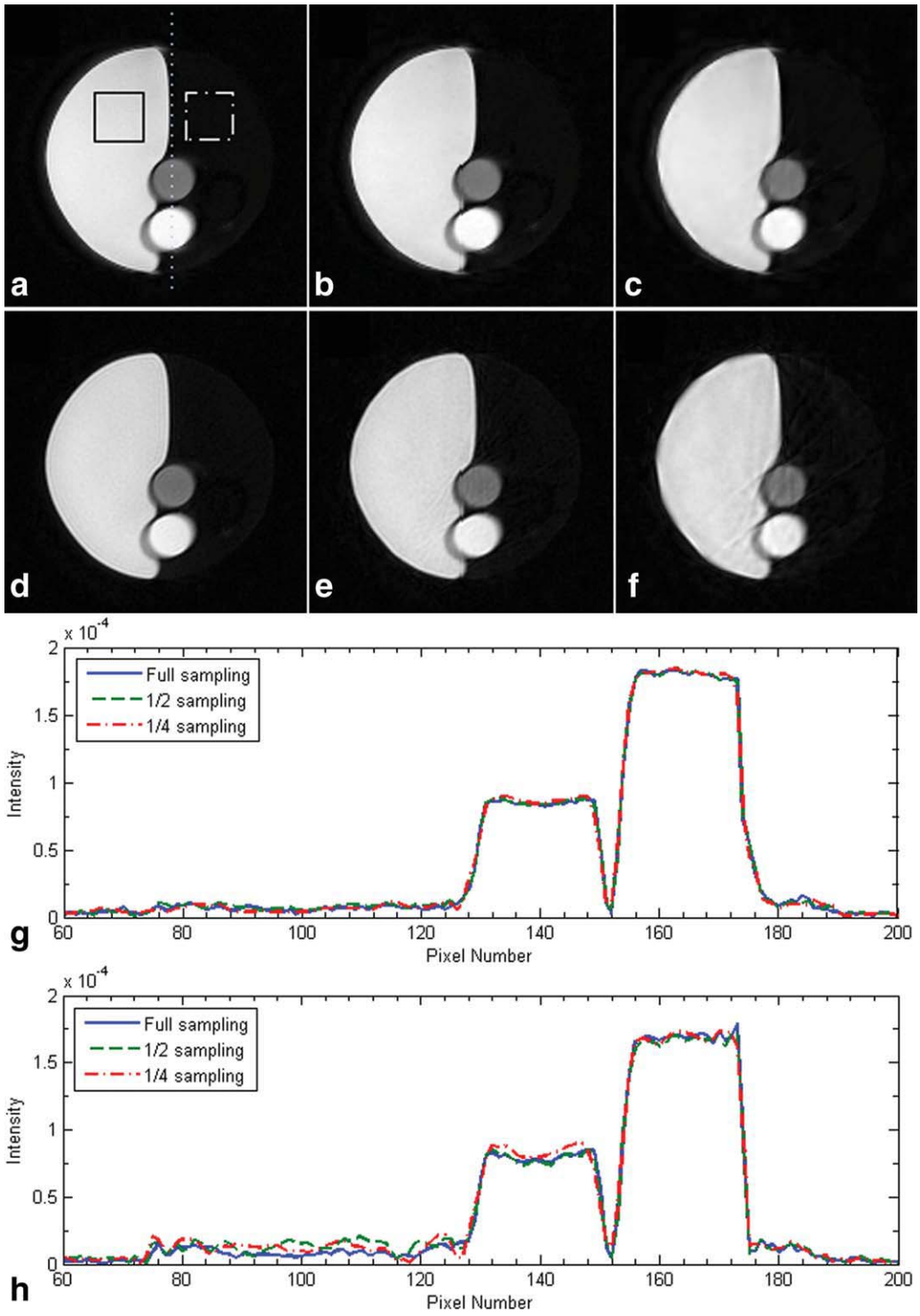

FIG. 7. The reconstruction results of the water–oil phantom. **a–c:** Water images using the proposed method (with $\lambda_1 = 0.01$ and $\lambda_2 = 0.01$, 10 inner iterations and eight outer iterations), with full sampling (ETL = 19 and 22 blades), with 1/2 sampling, and with 1/4 sampling, respectively. The sum of value of the pixels in the solid box is divided by the one in the dash–dot box, which delivers the ratio of the water signal to the remaining fat signal (R). The SD of value of pixels in the dash–dot box is calculated. R and SD of different patterns are tabulated in Table 5; **d–f:** Water images using the regridding method, with the same patterns used in a–c; **g:** The profiles of a–c along the dot line in a; **h:** The profiles of d–f along the dot line in a. The water signal in h is noisy. The remaining fat signal in h is higher than that in g.

number of blades of an undersampled BLADE acquisition needs to be balanced between scan time and the spatial resolution request of the imaged objects. For instance, as imaging brain, the image quality is acceptable when reducing the number of blades to 1/4 of the number of the fully sampled data set.

The strategies reducing scan time by reducing the number of blades may benefit some low performance systems.

Table 5
Ratio of the Water Signal and the Remaining Fat Signal (R), the SD of the Remaining Fat Signal Using the Proposed Algorithm and the Regridding Method, Under Case 1 (Full Sampling), Case 2 (1/2 Sampling), and Case 3 (1/4 Sampling)

Sampling pattern	R with iterative method	R with regridding method	SD with iterative method	SD with regridding method
Full sampling	25.2	24.7	4.9e-008	6.8e-008
1/2 sampling	25.1	24.3	5.0e-008	8.7e-008
1/4 sampling	25.5	22.2	4.5e-008	1.2e-007

On these systems, because of the limitation of the gradient system performance, the time spacing τ for phase offset π (2.37 msec at 1.5T) may not be reachable. Therefore, the three echoes are not able to fit into one bipolar acquisition. In this case, the monopolar readout scheme is needed after two separate excitations. As a result, the scan time will be doubled. It is needed to reduce the scan time by reducing the number of blades so as to limit impacts from the motions between excitations.

With simulation, we observed that the regularized iterative method had denoising characteristic because of the performance of TV function, as stated by other reports (31,34,40). Furthermore, we observed another phenomenon that the SNR of the images using the regularized iterative reconstruction decrease faster than the regridding method when increasing number of blades. We supposed that the regularized iterative method is not severely sensitive to the accumulative random noise, when the weighting factor of TV is specified. The total energy of the noise increases with increasing the number of samples, which results in an apparent SNR reduction in the final images. This is further proved by an additional experiment changing the variance of white gaussian noise from 0.001 to 0.05, using six blades. The SNR with the regularized iterative method ($\lambda_1 = 0.001$ and $\lambda_2 = 0.01$) is 3.2; the SNR of true object is 1.5 and the SNR with the regridding method is 2.5. It is improved when increasing the weighting factor of TV function, as shown in Table 4. It is slightly improved when increasing the number of iterations, as note "a" under Table 4. This is because that the convergence performance of the iterative reconstruction keeps reducing slowly after certain iterations. How to select an appropriate weighting factor of TV is a tradeoff between SNR improvement and the preservation of the fine structures, as stated for an undersampled radial trajectory by Block et al. (31). For example, for the phantom studies, $\lambda_1 = 0.01$ was used; whereas, $\lambda_1 = 0.001$ was used in the in vivo experiments to preserve the nonuniformly distributed anatomies.

The NMSE convergence curve of the noise-free simulation shows that the regularized iterative reconstruction algorithm converges very fast at the first iterations and then keeps reducing very slowly. According to this behavior, the tolerance for the stopping criterion was tried to be a low value when the algorithm converges slowly, e.g., 0.0001 in the simulation studies. We observed that this tolerance setting did not help to obtain significant improvement on image quality. In practice, the image quality is acceptable by setting appropriate number of iterations. The number of iterations results from the optimal compromise between the image quality and the time cost of reconstruction.

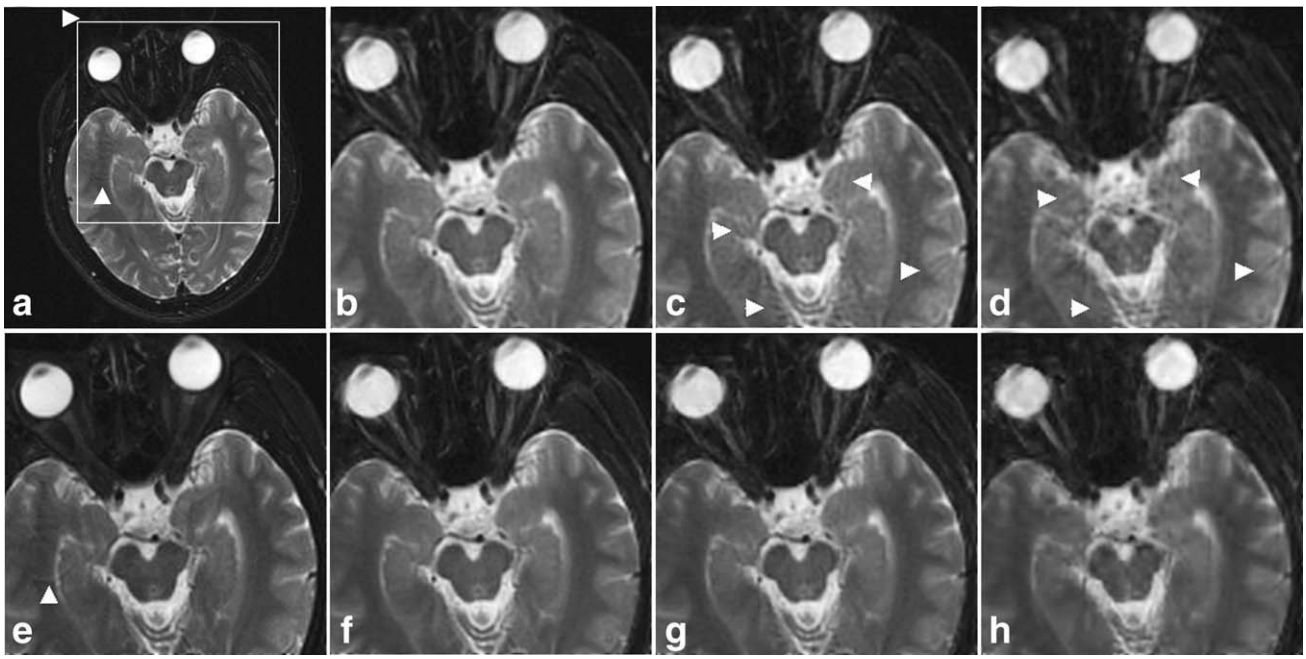

FIG. 8. The reconstruction results of the orbit image on volunteer. **a:** Image of TSE with fatsat. Artifact from eye-ball motion can be seen in the phase-encoding direction. For other results, the region in the box is zoomed; **b–d:** Zoomed water images using the regridding method, with full sampling (ETL = 19 and 22 blades), with 1/2 sampling and with 1/4 sampling, respectively. Streaking artifacts can be seen in c and d (as pointed by arrows); **e:** Zoomed water image of TSE three-point Dixon. Motion artifact from eye ball can be seen in the phase-encoding direction (as pointed by arrow); **f–h:** Zoomed water images using the proposed method (with $\lambda_1 = 0.001$ and $\lambda_2 = 0.01$, 10 inner iterations and eight outer iterations), with the same patterns in b–d.

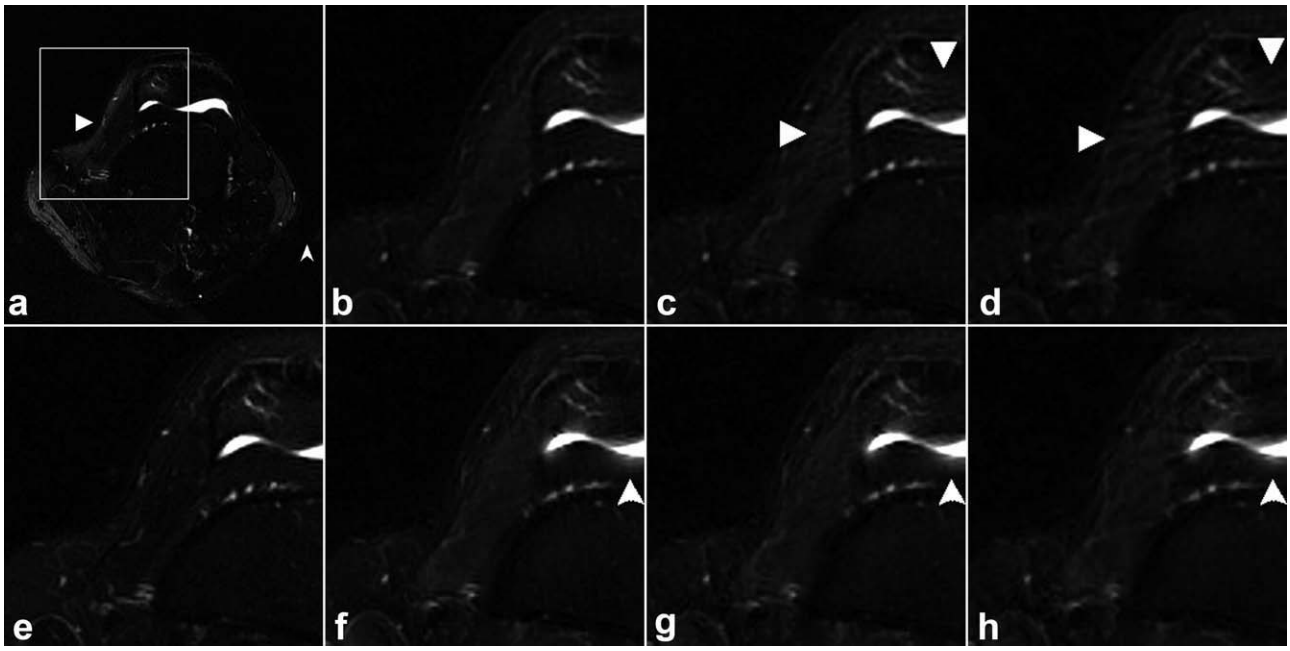

FIG. 9. The reconstruction results of the knee image on volunteer. **a:** Image of TSE with fatsat. Pulsation artifacts can be seen in the phase-encoding direction. Fat signal was not suppressed well because of the local B_0 inhomogeneities. For other results, the region in the box is zoomed; **b–d:** Zoomed water images using the regridding method, with full sampling (ETL = 17, 24 blades), with 1/2 sampling and with 1/3 sampling, respectively. The streaking artifacts can be observed, as pointed by arrows. **e:** Zoomed water image of TSE three-point Dixon; **f–h:** Zoomed water images using the proposed method (with $\lambda_1 = 0.001$ and $\lambda_2 = 0.01$, 10 inner iterations and eight outer iterations), using the same schemes in b–d. Slight blurring can be seen in image f,g, as pointed by arrows.

The regularized iterative reconstruction works equally well on complex images, which is essential for water–fat separation. All images reconstructed with our proposed method separated water–fat very well. The TSE BLADE three-point Dixon sequence inherits the motion robustness of BLADE. This advantage is demonstrated in Figs. 8 and 9, when comparing the images from our proposed method with those from a TSE three-point Dixon sequence and a TSE sequence with spectral fatsat with Cartesian *k*-space sampling.

In our in vivo study, we noticed slight blurring (as indicated by the arrows in Fig 9f–h). This artifact predominantly occurs around hyperintense structures. We suspect that it is an averaging effect for sparse structures with our imaging and reconstruction technique. We found that such blurring was influenced by the window size of the interpolation used in the max–min nonuniform fast Fourier transform method. In the case of the knee, blurring is reduced when a smaller window size is used.

The computational requirements for our proposed method are higher than that of the conventional regridding method. The reconstruction time per image (matrix size 256 × 256, 10 outer iterations and 10 inner iterations, seven blades, ETL = 19 and 8 channels) using MATLAB codes was 4 min 50 sec. In contrast, it took only 20 sec for the regridding algorithm. This issue of the reconstruction speed can be improved by optimizing the algorithm (e.g., reducing the number of loops, introducing the parallel computation technique), by introducing new computation technologies (41), or by using other optimization methods, like the Bregman iteration (32,33).

CONCLUSIONS

We introduced a method combining regularized iterative reconstruction with water–fat separation using the multipoint Dixon technique and the BLADE trajectory. The approach can handle the data from different multichannel coils and recover the image using general a priori knowledge of the tissue structure of the objects by using penalty functions, the TV function and the wavelet function. The proposed method shows good suppression on streaking artifacts, when compared with a conventional regridding method, and results in better preservation of fine structures. These advantages would be relevant to clinical applications. The computational performance of the proposed algorithm is modest and may be optimized for speed by known technical approaches.

ACKNOWLEDGEMENTS

The authors thank Dr. Yiu-Cho Chung for fruitful discussions and kind assistance in manuscript revision.

REFERENCES

1. Haase A, Frahm J, Hanicke W, Matthaei D. 1H NMR chemical shift selective (CHESS) imaging. Phys Med Biol 1985;30:341–344.
2. Geen H, Freeman R. Band-selective radiofrequency pulses. J Magn Reson 1991;93:93–141.
3. Schick F, Forster J, Machann J, Huppert P, Claussen CD. Highly selective water and fat imaging applying multislice sequences without sensitivity to B_1 inhomogeneities. Magn Reson Med 1997;38: 269–274.
4. Schick F. Simultaneous highly selective MR water and fat imaging using a simple new type of spectral-spatial excitation. Magn Reson Med 1998;40:194–202.

5. Meyer CH, Pauly JM, Macovski A, Nishimura DG. Simultaneous spatial and spectral selective excitation. Magn Reson Med 1990;15: 287–304.
6. Block W, Pauly J, Kerr A, Nishimura D. Consistent fat suppression with compensated spectral-spatial pulses. Magn Reson Med 1997;38:198–206.
7. Atlas SW, Grossman RI, Hackney DB, Goldberg HI, Bilaniuk LT, Zimmerman RA. STIR MR imaging of the orbit. AJR Am J Roentgenol 1988;151:1025–1030.
8. Baker LL, Goodman SB, Perkash I, Lane B, Enzmann DR. Benign versus pathological compression fractures of vertebral bodies—assessment with conventional spin-echo, chemical-shift, and stir MR imaging. Radiology 1990;174:495–502.
9. Bakker CJ, Witkamp TD, Janssen WM. Short TI short TR inversion recovery imaging using reduced flip angles. Magn Reson Imaging 1991;9:323–330.
10. Dixon WT. Simple proton spectroscopic imaging. Radiology 1988; 153:189–194.
11. Glover GH, Schneider E. Three-point Dixon technique for true water fat decomposition with B_0 inhomogeneity correction. Magn Reson Med 1991;18:371–383.
12. Glover GH. Multipoint Dixon technique for water and fat proton and susceptibility imaging. J Magn Reson Imaging 1991;1:521–530.
13. Szumowski J, Coshow WR, Li F, Quinn SF. Phase unwrapping in the 3-point Dixon method for fat-suppression MR-imaging. Radiology 1994;192:555–561.
14. Hardy PA, Hinks RS, Tkach JA. Separation of fat and water in fast spin-echo MR-imaging with the 3-point Dixon technique. J Magn Reson Imaging 1995;5:181–85.
15. Xiang QS, An L. Water–fat imaging with direct phase encoding. J Magn Reson Imaging 1997;7:1002–1015.
16. Coombs BD, Szumowski J, Coshow W. Two-point Dixon technique for water–fat signal decomposition with B_0 inhomogeneity correction. Magn Reson Med 1997;38:884–889.
17. Skinner TE, Glover GH. An extended two-point Dixon algorithm for calculating separate water, fat, and B_0 images. Magn Reson Med 1997;37:628–630.
18. Wang Y, Li DB, Haacke Brown JJ. A three-point Dixon method for water and fat separation using 2D and 3D gradient-echo techniques. J Magn Reson Imaging 1998;8:703–710.
19. Reeder SB, Wen Z, Yu H, Pineda AR, Gold GE, Markl M, Pelc NJ. Multicoil Dixon chemical species separation with an iterative least-squares estimation method. Magn Reson Med 2004;51:35–45.
20. Lu WM, Yu HZ, Shimakawa A, Alley M, Reeder SB, Hargreaves BA. Water–fat separation with bipolar multiecho sequences. Magn Reson Med 2008;60:198–209.
21. Reeder SB, Pineda AR, Wen Z, Shimakawa A, Yu H, Brittain G, Beaulieu CH, Pelc NJ. Iterative decomposition of water and fat with echo asymmetry and least-squares estimation (IDEAL): application with fast spin-echo imaging. Magn Reson Med 2005;54:636–644.
22. Huo DL, Li ZQ, Aboussouan E, Karis JP, James G. Pipe JG. Turboprop IDEAL: a motion-resistant fat–water separation technique. Magn Reson Med 2009;61:188–195.
23. Pipe JG. Motion correction with PROPELLER MRI: application to head motion and free-breathing cardiac imaging. Magn Reson Med 1999;42:963–969.
24. Jackson JI, Meyer CH, Nishimura DG, Macovski A. Selection of a convolution function for Fourier inversion using gridding. IEEE Trans Med Imaging 1991;10:473–478.
25. Pipe JG, Menon P. Sampling density compensation in MRI: rationale and an iterative numerical solution. Magn Reson Med 1999;41:179–186.
26. Arfanakis K, Tamhane AA, Pipe JG, Anastasio MA. *k*-Space undersampling in PROPELLER imaging. Magn Reson Med 2005;53:675–683.
27. Walsh DO, Gmitro AF, Marcellin MW. Adaptive reconstruction of phased array MR imagery. Magn Reson Med 2000;43:682–690.
28. Candes EJ, Romberg J, Tao T. Robust uncertainty principles: exact signal reconstruction from highly incomplete frequency information. IEEE Trans Inform Theory 2006;52:489–509.
29. Sidky EY, Kao CM, Pan XC. Accurate image reconstruction from few-views and limited-angle data in divergent-beam CT. J X-Ray Sci Tech 2006;14:119–139.
30. Lustig M, Lee JH, Donoho DL, Pauly JM. Fast imaging with randomly perturbed undersampled spirals and l1 reconstruction. In: Proceedings of the 13th annual meeting of ISMRM, Miami, Florida; 2005. p. 685.
31. Block KT, Uecker M, Frahm J. Undersampled radial MRI with multiple coils. Iterative image reconstruction using a total variation constraint. Magn Reson in Med 2007;57:1086–1098.
32. Chang T-C, He L, Fang T. MR image reconstruction from sparse radial samples using Bregman iteration. In: Proceedings of the 14th annual meeting of ISMRM, Seattle, WA; 2006. p. 696.
33. Liu B, King K, Steckner M, Xie J, Sheng JH, Ying L. Regularized sensitivity encoding (SENSE) reconstruction using Bregman iterations. Magn Reson Med 2009;61:145–152.
34. Rudin LI, Osher S, Fatemi E. Nonlinear total variation based noise removal algorithms. Physica D 1992;60:259–268.
35. Taubman D, Marcellin M. JPEG2000: image compression fundamentals standards and practice. Beijing: Publishing House of Electronics Industry; 2004.
36. Daubechies I. Orthonormal bases of compactly supported wavelets. II. Variations on a theme. SIAM J Math Anal 1993;24:499–519.
37. Hestens MR, Stiefel E. Methods of conjugate gradients for solving linear systems. J Res Natl Bur Stand 1952;49:409–436.
38. Fessler JA. Nonuniform fast Fourier transforms using min–max interpolation. IEEE T-SP 2003;51:560–574.
39. Zhou K, Zaitsev M, Bao S. Reliable two-dimensional phase unwrapping method using region growing and local linear estimation. Magn Reson Med 2009;62:1085–1090.
40. Strong D, Chan T. Edge-preserving and scale dependent properties of total variation regularization. Inst Phys Publ Inverse Probl 2003;19: S165–S187.
41. Murphy M, Keutzer K, Vasanawala S, Lustig M. Clinically feasible reconstruction time for L1-SPIRiT parallel imaging and compressed sensing MRI. In: Proceedings of the 19th annual meeting of ISMRM, Stockholm, Sweden; 2010. p. 4854.